

RESEARCH ARTICLE

10.1029/2019JB017448

TX2019slab: A New *P* and *S* Tomography Model Incorporating Subducting Slabs

 Chang Lu¹ , Stephen P. Grand¹, Hongyu Lai² , and Edward J. Garnero²
¹Department of Geological Sciences, Jackson School of Geosciences, University of Texas at Austin, Austin, TX, USA,²School of Earth and Space Exploration, Arizona State University, Tempe, AZ, USA**Key Points:**

- We developed new *P* and *S* tomography models incorporating 3-D subducting slabs
- Mislocation effects caused by subducting slabs were reduced by inverting for velocity and source location simultaneously
- The spin transition and the post-perovskite phase transition may explain lower mantle heterogeneities

Supporting Information:

- Supporting Information S1

Correspondence to:C. Lu,
lcer.js@utexas.edu**Citation:**

Lu, C., Grand, S. P., Lai, H., & Garnero, E. J. (2019). TX2019slab: A new *P* and *S* tomography model incorporating subducting slabs. *Journal of Geophysical Research: Solid Earth*, 124, 11,549–11,567. <https://doi.org/10.1029/2019JB017448>

Received 26 JAN 2019

Accepted 27 SEP 2019

Accepted article online 22 OCT 2019

Published online 11 NOV 2019

Abstract Large numbers of earthquakes occur in subduction zones that are marked by dipping, narrow high seismic velocity slabs. The existence of these fast velocity slabs can cause serious earthquake mislocation problems that can bias estimates of seismic travel time residuals. This can affect the recovery of subducting slabs in tomography as well as introduce significant artifacts into lower mantle structure in tomography models. In order to better account for known subducting slabs, we performed a new *P* and *S* wave joint tomography inversion incorporating a three-dimensional thermal model of subducting slabs in the starting model. In addition, velocity and source locations were inverted for simultaneously. Our new *P* and *S* models feature higher-amplitude subducting slabs compared with previous global tomography results. The *S* to *P* heterogeneity ratio based on the new tomography model indicates that thermal elastic effects alone cannot explain all the heterogeneities in the lower mantle. Much of the observed abnormal *S* to *P* heterogeneity ratio can be explained by anelastic effects, the spin transition, and phase transitions of bridgmanite to post-perovskite in the lower mantle.

Plain Language Summary Seismic tomography uses seismic travel time data to image deep earth velocity structure. However, it has been shown that the existence of subducting slabs can significantly bias the imaging result. In order to reduce this effect, we produced a new *P* and *S* wave tomography model that included theoretical three-dimensional subducting slab structures in the starting model. The new model has higher-amplitude subducting slabs compared with other models. Based on the new model, we conclude that it is difficult to explain the *P* and *S* velocity anomalies found in the deep mantle by temperature variations alone without invoking complex mineral phase transitions, large anelastic effects, or chemical variations.

1. Introduction

Subduction of oceanic lithosphere is believed to play a critical role in large-scale mantle convection (e.g., Billen, 2008; Kellogg et al., 1999). The investigation of deep subducting slabs, therefore, has been an active field in geophysics. It is widely accepted that subducting slabs are relatively cold and thus have high seismic velocity compared to surrounding mantle (e.g., Fukao & Obayashi, 2013; Zhao et al., 2017). Global seismic tomography, a method to image deep earth seismic velocity structure, has been used to constrain the location of subducting slabs. Generally, shear wave global tomography has limited ability to image short-wavelength structures such as subducting slabs (e.g., French & Romanowicz, 2014; Grand, 2002; Kustowski et al., 2008; Moulik & Ekström, 2014; Panning & Romanowicz, 2006; Ritsema et al., 2011). Compressional wave global tomography has provided higher-resolution images of upper mantle slabs (e.g., Amaru, 2007; Li et al., 2008; Obayashi et al., 2013; Simmons et al., 2012). However, detailed waveform modeling studies suggest that the amplitude of subducting slabs is underestimated in global *P* wave tomography models (Zhan et al., 2014). Tao et al. (2018) performed full-waveform inversion using upper mantle triplicated waves to image the subducting slabs beneath Eastern Asia. Both of their *P* and *S* models show much higher-amplitude velocity anomalies inside the slabs than in global tomography models. Other seismic modelling results, as well as theoretical thermal models of subducting slabs, also imply far stronger velocity anomalies within slabs relative to those seen in global tomography (Chen et al., 2007; Kawakatsu & Yoshioka, 2011; Syracuse et al., 2010; Wang et al., 2014). The discrepancies between detailed seismic studies of slabs with global tomography models imply a potential problem with using tomography models to infer density anomalies for use in mantle convection studies.

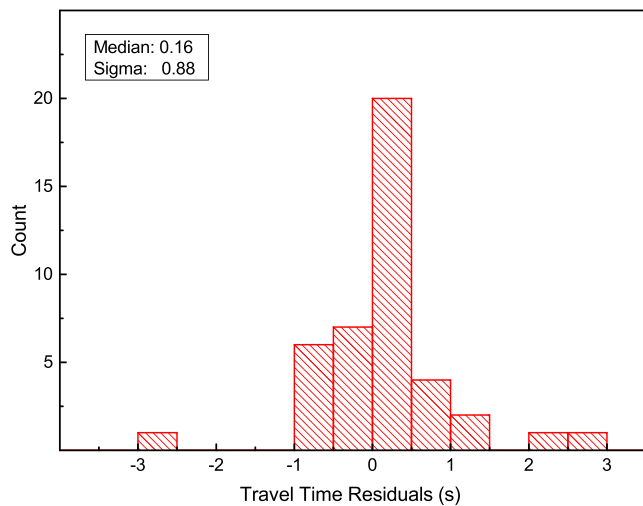


Figure 1. Distribution of travel time residuals measured at station MAW for a representative 30×30 -km earthquake group used in the EHB data selection process. The group is centered at 7.3°S , 155.9°E , and 45-km depth. The station MAW is located in Antarctica 67.6°S , 62.9°E . The residuals outside $\pm 2\sigma$ were treated as outliers and eliminated from the inversion.

The existence of sharp, dipping fast velocity anomalies can also bias earthquake locations and impact seismic travel time data used in tomography (Creager & Jordan, 1984; Ding & Grand, 1994; Sleep, 1973). Therefore, the incorrect imaging of subducting slabs could degrade tomography models even far from subduction zones. Through synthetic testing, Lu and Grand (2016) found that the incorrect imaging of subducting slabs could introduce up to 0.5% amplitude false velocity anomalies in the lower mantle in global shear wave tomography. This is comparable to the amplitude of velocity anomalies found in the lower mantle. These artifacts may have significant implications for interpretation of lower mantle heterogeneities. For example, some studies use the S to P heterogeneity ratio to identify potential chemically distinct heterogeneities (e.g., Koelemeijer et al., 2016; Masters et al., 2000; Saltzer et al., 2001; Tesoniero et al., 2016). Artifacts produced by incorrectly accounting for subducting slabs can impact the reliability of results using this approach.

Lu and Grand (2016) compare several strategies to best account for subducting slabs in global tomography. They suggest including a priori subducting slabs in the starting model and performing structure and source location jointly in tomographic inversions. In this study, we present a new P and S global tomography model using a three-dimensional (3-D) subducting slab structure in the initial model. This enables us to produce

a global tomography model with more realistic subducting slabs. In the lower mantle, we evaluate the effect of subducting slabs on S to P heterogeneity ratio estimation.

2. Data and Method

2.1. P Wave Data

The P wave data used in this study are from the database of travel time residuals maintained by E. R. Engdahl and coworkers (EHB data; Engdahl et al., 1998). They use arrival times reported to the International Seismological Center (ISC) and the U.S. Geological Survey's National Earthquake Information Center (NEIC), relocate earthquakes and re-identify phases, and then produce a final data set after quality control. In this study, we use P , pP , and Pn phases in the EHB data, which contains approximately 14 million rays from $\sim 553,000$ earthquakes from the years 1966 to 2008.

Even though the quality of EHB data is significantly higher than the raw ISC catalogue data, there are still errors in the data set. For example, we have found cases where two nearby earthquakes have more than a 10-s difference in travel time residuals to a common station. In order to further improve the data quality, we designed a new data selection process for the EHB data. We first group nearby earthquakes together, then evaluate the travel time residuals of each group at each station. For earthquakes close to subduction zones, a group covers about a 30×30 -km area in the horizontal direction, while larger 300×300 -km areas form groups away from subduction zones. In the radial direction, we separate earthquakes using a 30-km interval. Figure 1 shows the distribution of travel time residuals for a representative 30×30 -km group (centered at 7.3°S , 155.9°E ; 45-km depth) to station MAW in Antarctica (67.6°S , 62.9°E). The residuals outside $\pm 2\sigma$ (corresponding to $\sim 95\%$ confidence interval) were labeled as outliers and eliminated from the inversion. For groups with very few arrivals to a station (less than 10 arrivals), the standard deviation of the whole EHB data (~ 1.8 s) is used to define outliers. This process rejected about 5% of the EHB data.

2.2. S Wave Data

We include two groups of shear wave data in this study. The first group (TX data) was used in Lu and Grand (2016). The data set consists of $\sim 70,000$ global S, ScS, SKS, and SKKS phase travel times from 540 earthquakes. Their upgoing and surface bounce equivalents are also included. Upper mantle triplicated waves are also included to provide better coverage in the upper mantle and transition zone. All the travel times were manually measured using a seismic waveform approach. The data measurement method, with examples, is discussed in Grand (1994). The other group of shear wave data is presented in Lai et al. (2019). They use a semiautomated process to determine the onset time of horizontally polarized shear waves bandpassed

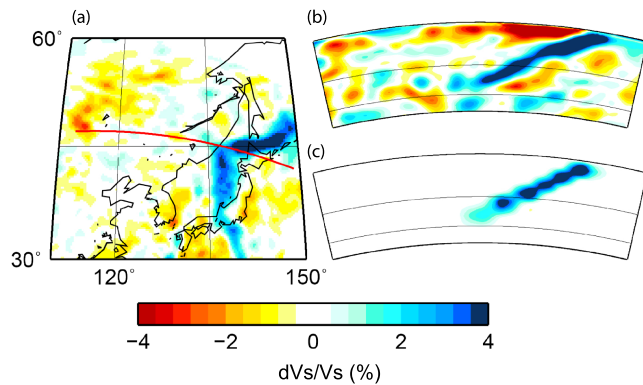


Figure 2. Comparison of the subducting slab beneath East Asia found in a regional tomography model FWEA18 (Tao et al., 2018) and our input slab model. (a) Horizontal slice of shear wave model FWEA18 at 300 km. The red line shows the location of the cross sections in (b) and (c). (b) Cross section of the same tomography model in (a). (c) Cross section of the input shear wave slab model. Solid black lines represent the 410- and 660-km discontinuities, respectively.

from 0.01 to 0.1 Hz. The measurements involve the derivation of an empirical wavelet, which is matched to seismic waveforms from a given earthquake, through an iterative cross-correlation process. The onset travel time is measured based on a Gaussian function which best fits the empirical wavelet. This data set includes ~226,000 S, SS, SSS, ScS, and ScSScS phases from 360 earthquakes all of which turn within the lower mantle; that is, upper mantle triplicated phases are excluded. These new data provide better ray coverage than the first data set in the lower mantle, especially in the southern hemisphere (Figure S1).

2.3. Input Slab Model

We use a starting 3-D slab model based on a theoretical global 3-D thermal model of subducting slabs given by Stadler et al. (2010). The slab locations are defined by seismicity and represented on a $0.1^\circ \times 0.1^\circ$ grid. The model does not include seismically inactive subduction zones so it is a relatively conservative representation of slabs. The geometry of the slabs has been checked against model Slab 1.0 (Hayes et al., 2012). The high degree of similarity between the two models, in terms of slab geometry, confirm the reliability of the input slab model. The thermal structure of the slab model is determined by the age of the subducting plate at the time of sub-

duction and the convergence rate. When compared with slab thermal models produced by detailed dynamic modeling (e.g., Kawakatsu & Yoshioka, 2011; Syracuse et al., 2010; van Keken et al., 2011), the Stadler et al. model generally has larger thermal anomalies. Therefore, we changed the thermal anomalies in the Stadler et al. model using the slab thermal model of van Keken et al. (2011) while keeping the geometry the same. Because the van Keken et al. model only contains 2-D thermal structures across different subducting slabs, we interpolated their model for each slab in Stadler et al.'s model to make the average thermal anomaly across slabs to be consistent with van Keken et al.'s model. The scaling we used to adjust the amplitude of the Stadler et al. model varied from ~ 0.7 to ~ 0.9 .

We followed Lu and Grand (2016) to convert the thermal slab model to a 3-D perturbation model of P and S velocity. The slab model contains uncertainties due to both the thermal structure as well as the mineral physics modeling procedure. However, our derived slab model generally agrees with some detailed regional studies (e.g., Chen et al., 2007; Gaherty et al., 1991; Tao et al., 2018; Vidale, 1987) in terms of geometry as well as seismic amplitudes. In Figure 2, we compare our input slab model for a cross section in East Asia with a recent regional full-waveform tomography model FWEA18 (Tao et al., 2018). Both models have about a 100-km-thick undeformed subducting slab dipping to 660-km depth. Therefore, we feel the model is a good first-order approximation to global slab structure.

2.4. Forward Modeling

In our previous work, we used the open-source package “SPECFEM3D GLOBAL” Spectral-Element Method (SEM; Komatitsch & Tromp, 2002a, 2002b) to model the effect of the 3-D subducting slabs on shear wave travel times for the handpicked data set discussed above (Lu & Grand, 2016). For each earthquake, we computed SEM synthetics for the 1-D starting model then another simulation for a second model that included slabs embedded in the 1-D model. The calculations are accurate to periods of about 12 s. Comparing the two simulations, for each measured phase in the data, allowed us to adjust the travel time residuals for the effect of the slabs. In other words, we produce a set of residuals relative to an Earth model with slabs.

For the presumably higher frequency and far larger EHB data, it is not feasible to use the SEM method to model the effect of slabs on the data. Therefore, instead of using SEM, we used 3-D ray tracing to evaluate the effect of slabs on our P wave data. The shear wave data set from Lai et al. (2019) are measurements of onset time so are presumably the equivalent of high-frequency travel times. Thus, we also used 3-D raytracing to correct the Lai et al. data set for slab structure. The open-source LLNL-Earth3D 3-D ray tracing package (Simmons et al., 2012) was used for this purpose. The 3-D Earth can be represented by different levels of spherical tessellation grids. A higher tessellation recursion level means a finer grid and more computation cost. In order to check the accuracy of the 3-D ray tracing code as well as determine the optimal level of

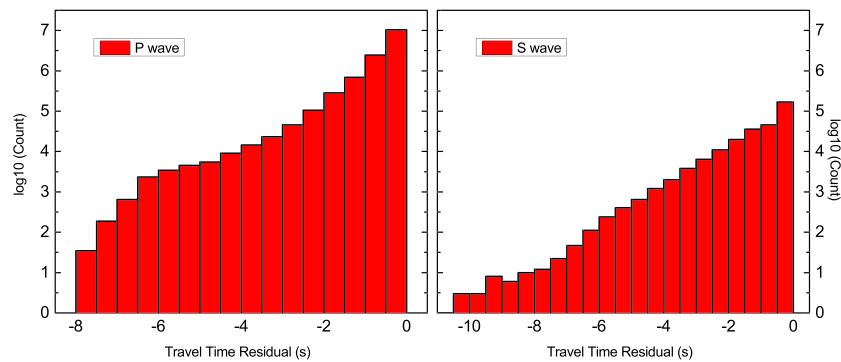


Figure 3. Distribution of travel time residuals caused by the input slab model. Plotted are the differences between a 1-D prediction of travel times and predictions for the same 1-D model with slabs embedded for all the data used in our inversion. *P* wave residuals were derived from 3-D ray tracing (Simmons et al., 2012), while the *S* wave residuals were obtained from 3-D ray tracing and SEM simulations (Komatitsch & Tromp, 2002a, 2002b).

the spherical tessellation grids, we compared 3-D ray tracing results with SEM simulation results for a few test earthquakes. We find that when the tessellation recursion level is above 9 (corresponding to ~ 0.25 arc degree average node spacing), the difference between 3-D ray tracing and SEM simulations agree to within 0.2 s, which we consider acceptable for our purposes. The effect of subducting slabs on the seismic travel time residuals are summarized in Figure 3. The largest travel time residual caused by our starting model is ~ 8 s for *P* wave data while it is ~ 12 s for *S* wave data.

The “TX” data set contains upper mantle turning waves. As discussed in Grand (1994), due to the large heterogeneity in the shallow mantle, at a given distance the ray paths of *S* or *SS* waves can be quite different depending on the specific region being sampled. Relative to standard 1-D models the difference is especially significant in cratonic regions. For this reason, different seismic models were used to determine ray paths for upper mantle waves in Grand (1994, 2002). This process required detailed waveform analysis, and thus is not suitable for large-volume catalogue data. The EHB *P* data set contains upper mantle turning waves. In order to correct the ray paths that sample cratonic regions for EHB data, we first derived a 3-D *S* wave craton model and then converted it to a *P* wave model (Figure S2). The fast velocity anomalies in our previous *S* wave tomography at the shallowest depths (Lu & Grand, 2016) are used to determine the location of cratons if they have Archean or Proterozoic crust (Laske et al., 2013). The fast velocity anomalies down to 210 km which are close to these regions are used to define the craton roots. These cold cratons are believed to have distinct chemical compositions relative to surrounding mantle and contain high percentages of Mg. Lee (2003) showed that the effect of Mg# ($100 \times \text{Mg}/(\text{Mg} + \text{Fe})$) on V_p/V_s ratio was significantly larger than the effect of temperature in peridotite. Therefore, we estimated the Mg# in cratons using a linear interpolation based on our *S* wave craton model, assuming that normal mantle has a low (87) Mg# while the fastest craton has the highest (94) Mg# (Lee, 2003). Using this approach, the average variation of Mg# in cratons is ~ 3.5 , which agrees with the value reported by Deschamps et al. (2002) and is slightly higher than predictions by Forte and Perry (2000) and Perry et al. (2003). Then we adopted the linear relationship between Mg# and V_p/V_s ratio reported by Lee (2003) to derive a *P* wave craton model. Using the *P* wave craton model, 3-D ray tracing (Simmons et al., 2012) was used to determine the ray paths for rays turning above 800-km depth (Figure S3). For rays turning below 800-km depth, the effect of cratons on seismic ray paths is negligible.

2.5. Joint *P* and *S* Inversion Starting From 3-D Slab

In our inversion, the mantle was divided into 99,146 blocks. The blocks are about 275×275 km in lateral dimension and vary from 75 to 240 km in thickness. Both *P* and *S* wave sensitivity kernels were calculated using the ray theory approximation based on a 1-D velocity model. For *S* waves, we use a combined TNA/SNA model (Grand & Helmberger, 1984), which is the same 1-D model as we used in previous TX models (Grand, 2002). The AK-135 model (Kennett et al., 1995) is used as the *P* wave starting model. The *P* and *S* wave data are known to have very different ray coverage, especially in the shallow mantle. At shallow depths, the *P* wave data have limited sampling of the oceans, while *S* wave data have much better resolution there. Therefore, we correlated the *P* wave and *S* wave models by introducing another term $X_{P/S}$ into our

inversion, which is the ratio of the P and S wave slowness perturbations in each layer. This parameter can be obtained using thermoelastic parameters from mineral physics measurements as a function of depth assuming a thermal origin for mantle seismic heterogeneity (see Lu & Grand, 2016 for details). The $X_{P/S}$ in cratons vary in 3-D and are consistent with the values used in our forward modeling. Also, Lu and Grand (2016) showed that correcting for earthquake mislocation can be better achieved if one inverts for velocity structure and earthquake location simultaneously. Therefore, we include earthquake location in our inversion as well. The linearized seismic tomography problem can be written as

$$\begin{bmatrix} G_P & & A_P \\ & \lambda G_S & \lambda A_S \\ D_P & & \\ & D_S & \\ \lambda_X & -\lambda_X X_{P/S} & \end{bmatrix} \begin{bmatrix} m_P \\ m_S \\ L_P \\ L_S \end{bmatrix} = \begin{bmatrix} r_P \\ \lambda r_S \\ 0 \\ 0 \\ 0 \end{bmatrix} \quad (1)$$

where G_P and G_S are the P and S wave sensitivity kernel matrices and r_P and r_S are the corresponding travel time residuals caused by velocity anomalies and earthquake mislocation. The travel time residuals r are the leftover residuals after we removed the effect of subducting slabs, which is the most significant difference from previous global tomography studies. We use λ to represent the relative weight of S wave data to P wave data. m_P and m_S are the P wave and S wave slowness perturbations and L represents the relocation parameters to be inverted that include changes in event latitude, longitude, and depth, as well as origin time. A is the relocation matrix formed of the partial derivatives for these parameters. D is a smoothing operator, which is a Laplacian filter with 76% of the weight applied to horizontal nearby blocks and 24% of the weight applied to the vertical nearby blocks. A weighting term λ_X is used to control how strong the connection between the P and S models is enforced. Through a trial and error process, λ_X was chosen to be 500 which was the maximum value before the connection term began to decrease the variance reduction of the S wave data (less than 0.5%; Figure S4).

3. Results

3.1. TX2019slab Model

We show our new model (TX2019slab) in horizontal slices at selected depths in Figure 4. The blocks used in the inversion and the input slab model have been resampled onto a $1^\circ \times 1^\circ$ grid when making the plot. Our P and S models generally agree with previous tomography results at large scale. At 150-km depth, our model shows fast velocity anomalies in cratonic regions as expected. Slow velocity anomalies are found beneath mid-ocean ridges as well as the East African Rift. Due to poor data coverage in the oceans, most previous global P wave tomography models do not have slow mid-ocean ridges (e.g., Amaru, 2007; Li et al., 2008; Obayashi et al., 2013). Our shallow oceanic P structure is mainly constrained by the S wave data and the relationship between P and S anomalies we introduced into the inversion. In the upper mantle and transition zone, short-wavelength subducting slabs appear to be the most heterogeneous structures in our model. Interestingly, the slab signature near 600-km depth is much broader than at 300-km depth. In the mid-lower mantle, as in previous tomography studies, two elongated fast velocity anomalies in P and S are seen beneath North/South America and South Asia. The locations of these fast anomalies generally agree with previous studies (e.g., Amaru, 2007; French & Romanowicz, 2014; Grand, 2002; Li et al., 2008; Moulik & Ekström, 2014; Obayashi et al., 2013; Ritsema et al., 2011). Beginning in the mid-lower mantle, slow anomalies are seen in both P and S beneath the south central Pacific and Africa. They increase in strength and size with depth and at the bottom of the mantle are quite broad. These two structures have been called Large Low Shear Velocity Provinces (LLSVPs; see Garnero et al., 2016 for a review). Note that the P wave amplitude is muted at the base of the mantle inside the Pacific LLSVP.

Our model yields a 33.8% overall variance reduction for the P wave data and 91.4% for S wave data. In comparison, we derived another P and S model using the same data, inversion method, and regularization but starting from a 1-D velocity model. We refer to this model as TX2019. The variance reduction, using model TX2019, is slightly less than 33.8% for the P wave data and 91.3% for the S wave data. The inversion starting

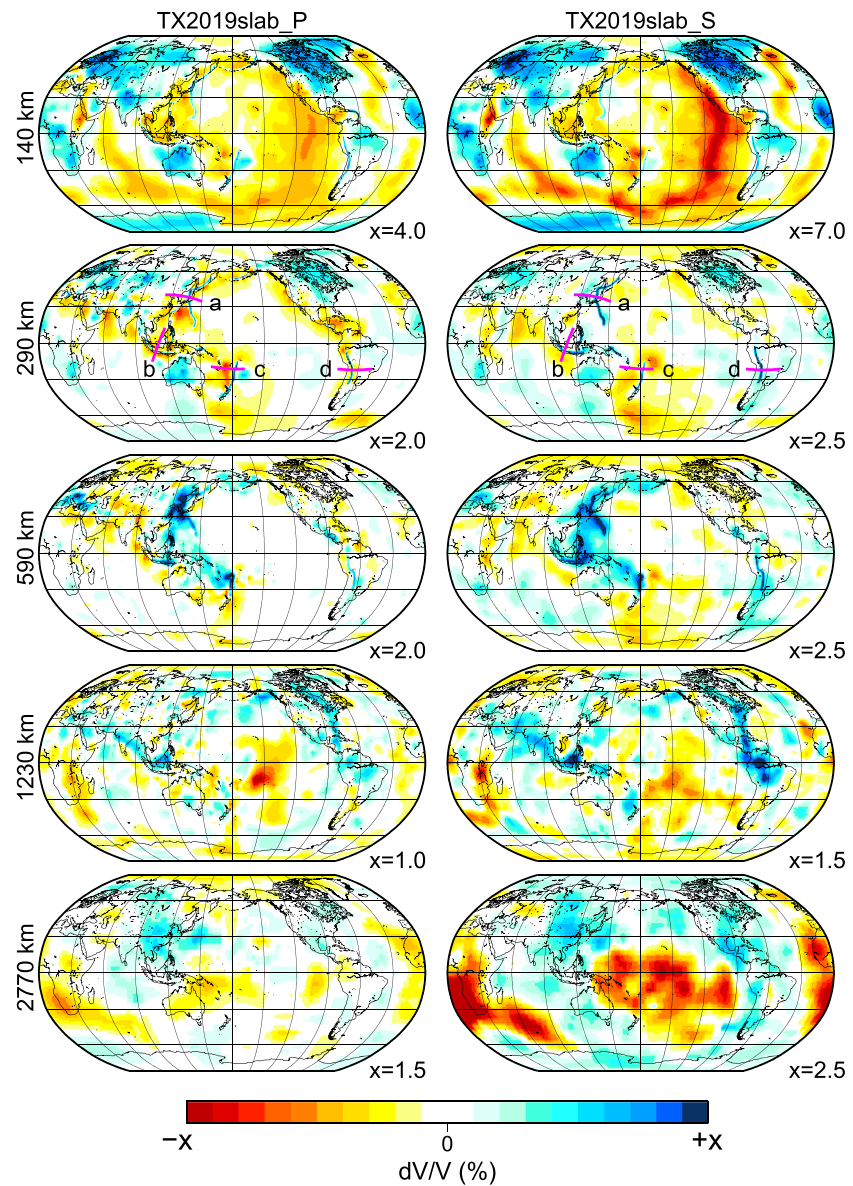


Figure 4. Lateral velocity variations in model TX2019slab at representative depths. Each row corresponds to the model at a particular depth, and the two columns show (left) *P* wave and (right) *S* wave models, respectively. The color scales change for each plot according to the amplitude (X) labeled at the bottom right corner. Purple lines in the second row show the locations of cross sections in Figures 7 and 8.

from a model with 3-D slabs results in a slightly better data fit than the inversion starting from the 1-D model although the difference is minimal. This is a clear indication of the nonuniqueness of models in global seismic tomography. The addition of slabs in our starting model, however, results in a model more consistent with regional studies and geodynamic models without sacrificing fit to global data.

3.2. Checkerboard Test

In order to test the ability of the data to image mantle structure, we performed a resolution test. The input checkerboard consists of $5^\circ \times 5^\circ$ blocks with alternating *P* wave velocity perturbations of $\pm 1.5\%$ for each layer. *S* wave velocity perturbations are scaled from the *P* wave, using the thermally introduced *S* to *P* relationship discussed above. Synthetic travel times were generated using the sensitivity matrix from forward modeling, and inverted using the same inversion scheme as for the real data (Figure 5). The correlation

coefficient (CC) between the input (m_{in}) and output models (m_{out}) at each depth has been calculated and labeled in Figure 5. The CC of two scalar fields can be calculated as

$$CC = \frac{\sum_{i=1}^N (X_{1,i} X_{2,i})}{\sqrt{\sum_{i=1}^N (X_{1,i})^2} \sqrt{\sum_{i=1}^N (X_{2,i})^2}} \quad (2)$$

where $X_{1,i}$ and $X_{2,i}$ are the i th elements in X_1 and X_2 after having mean values removed, respectively. We also calculated amplitude recovery (AR) to illustrate the resolution of the inversion. AR is defined as the ratio of the root-mean-square (RMS) amplitudes of m_{in} and m_{out} as

$$AR = \sqrt{\left(\sum_{i=1}^N m_{out}^2\right) / \left(\sum_{i=1}^N m_{in}^2\right)} \times 100\% \quad (3)$$

The CCs vary from 0.68 to 0.98, while amplitude recoveries are generally below 83% because of the regularization. Because of the S to PP wave velocity scaling used in the inversion, the shallow oceanic regions in the P wave model show some structures simply scaled from the S wave model. However, these regions are still the least resolved regions in the mantle. The derived P wave model in these regions highly depends on the S wave model as well as the scaling relationship used in the inversion.

3.3. Relocation Results

Earthquake hypocenters were relocated in our inversion. The average epicenter shift for the whole data set is about 9 km with a 6-km standard deviation. We also find an average 3 ± 10 -km depth shift for all the events used in our inversion. For the origin time, our inversion results found a 0.1 ± 1.2 -s average shift. These results generally agree with earthquake relocation results for EHB data reported by Amaru (2007). Figure 6 shows the shifts in event locations in two subduction regions. For better visualization, only earthquakes with more than 250 travel time residuals and a focal depth greater than 100 km are included in the plots. In regions that are azimuthally well sampled such as the Ryukyu arc and Izu-Bonin arc, the epicenter shifts are relatively small. In regions, such as South America, where the station coverage around the subduction zone is less complete, the epicenters shift more (Figure S5). Note that in the Kuriles, there is a systematic shift oceanward in epicenters due to the northwest dipping slab. There is also an interesting change in pattern along Central America that may be related to a change in slab dip angle along the subduction zone. Further analysis of the earthquake relocation results is left for future work.

4. Discussion

Compared with previous global tomography studies, the most significant difference in our model is that we performed our inversion starting with a 3-D subducting slab model and invert for velocity and earthquake location simultaneously. We compare our new model to previously published models in vertical cross sections across four major convergent plate boundaries. Figure 7 compares P models across the sections (Amaru, 2007; Li et al., 2008; Obayashi et al., 2013), and Figure 8 compares S models (French & Romanowicz, 2014; Moulik & Ekström, 2014; Ritsema et al., 2011). The cross-section locations are shown in Figure 4.

For the P wave models, similar fast anomalies are seen in all four tomography models (Figure 7). Across the northern Honshu arc, our model shows stagnant slab above the 660 discontinuity, and agrees with all the other models. The cross section across the western Java arc, beneath which the Indo-Australian plate is subducting, shows large fast anomalies in the uppermost lower mantle, with an extension of fast velocity into the deeper mantle to the north. Similar features can be seen in the other models, although our new model has a larger, stronger anomaly in the deepest mantle. The Tonga and South American cross sections show more differences among models. This is likely due to worse azimuthal station coverage around these regions. The cross sections across the Tonga arc show very complex structures. In our model, a stagnant slab above the 660 discontinuity is seen but there is also an anomaly in the lower mantle with a gap between the two. This is most similar to the GAPP4 model except in that model there is no gap between the deeper structure and the anomalies in the transition zone. Some studies (e.g., Bonnardot et al., 2009; Brudzinski & Chen, 2005) suggest that the stagnant slab above the 660 is the southwestward flattening of the downgoing slab

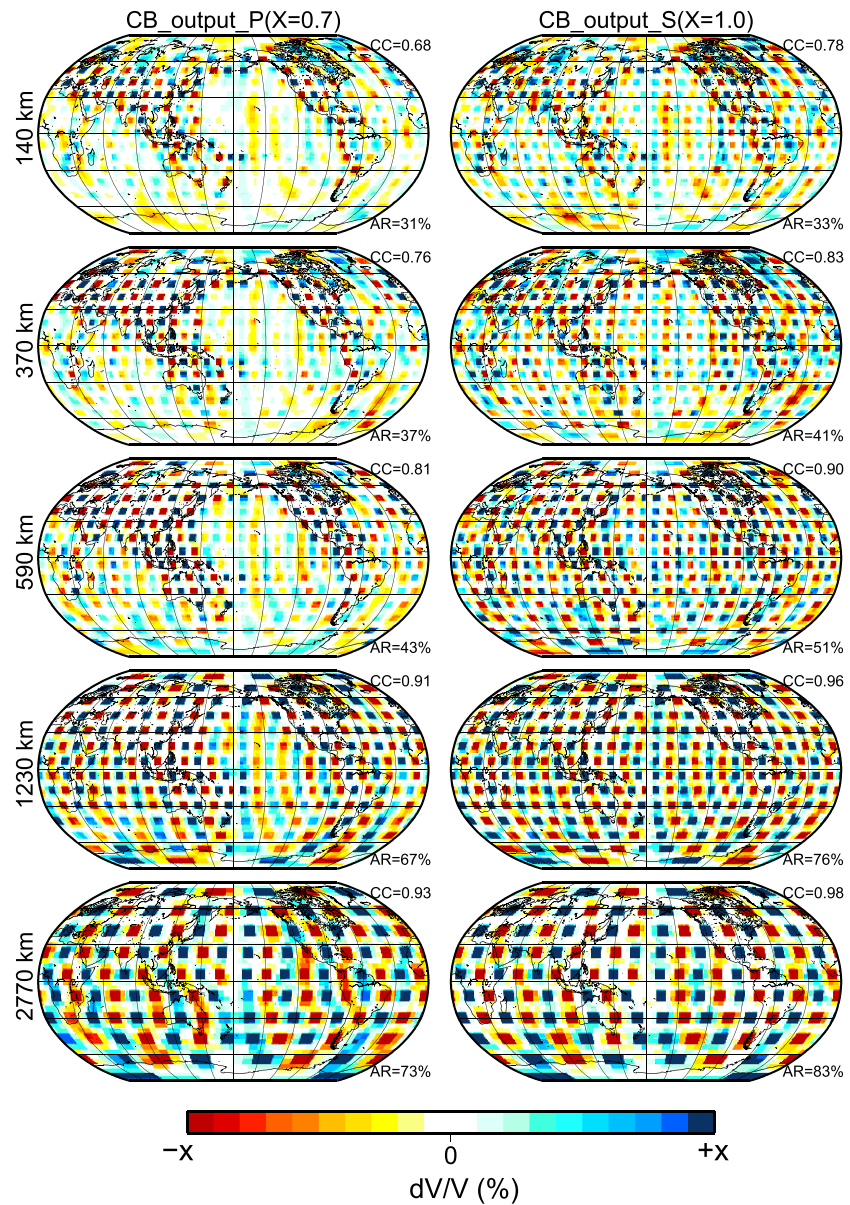


Figure 5. Output from a checkerboard test for (left column) P wave and (right column) S wave data at selected depths. Correlation coefficients (CCs) and amplitude recovery (AR) between the input checkerboard and the inversion results are labeled on each plot.

beneath the Lau basin, while the slab below the 660 is the westward extension of the downgoing slab from the southern Tonga trench (see Fukao & Obayashi, 2013, Figure 11). Richards et al. (2011), however, treat the stagnant slab above the 660 as a slab remnant detached from the Vanuatu trench. In South America, both our model and UU07P show a dipping slab in the upper mantle but the slab in our model penetrates deeper into the lower mantle. Possibly due to poor ray coverage, models GAPP4 and MIT08P have less clear subducting slabs in the upper mantle and little continuation of slab into the lower mantle.

Compared with the other models, the most significant difference with our model is the higher amplitude of velocity anomalies within subducting slabs. In our model, the amplitude of P wave velocity anomalies inside the slab in the upper mantle and transition zone are mostly higher than 2% while in the other models the anomalies are less than 1.5%. The difference is more significant in the regions where ray coverage is limited. The difference, of course, is because we include slabs in our starting model (Figure S6). The differences this

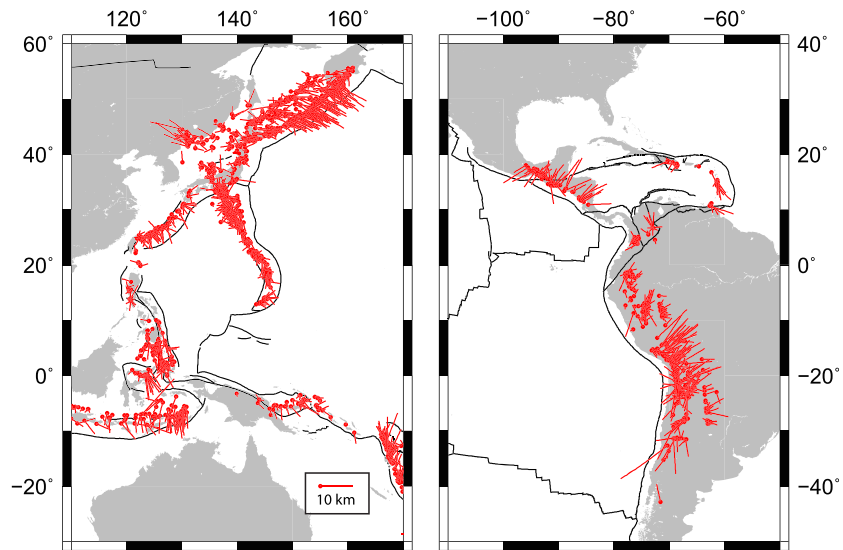


Figure 6. Representative epicenter shifts derived from velocity and source location joint inversion. The circles show the original earthquake epicenters. The red lines show the direction and amplitude of epicenter shifts. Only earthquakes with more than 250 travel time residuals and a focal depth greater than 100 km are shown for better visualization.

causes elsewhere in the model are smaller in amplitude but can still be significant. Given that the slabs in our model are consistent with regional studies and theoretical modeling, and that the data variance reduction is the same or slightly improved over a model derived without the slabs in the starting model, we feel that our new model has some advantages over previous models.

The comparison of our model with other *S* wave models also shows similar features (Figure 8). Generally, *S* wave models are longer wavelength and narrow slabs, such as in our model, are not well resolved. The slabs we start with are consistent with geologic inferences and also result in a slightly higher variance reduction of

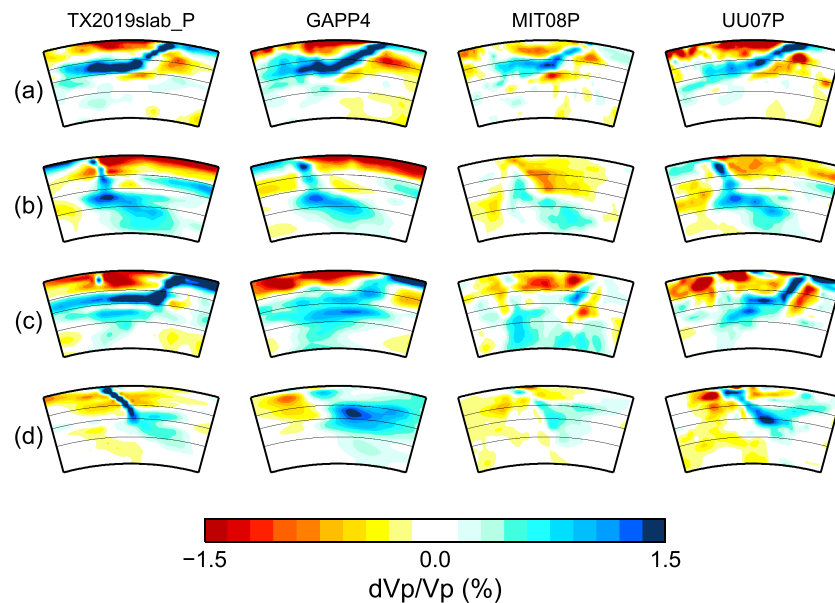


Figure 7. Comparison of cross sections across four major subduction zones in representative *P* wave tomography models. Each column shows specific tomography models, including TX2019_slab (this study), GAPP4 (Obayashi et al., 2013), MIT08P (Li et al., 2008), and UU07P (Amaru, 2007). Each row corresponds to cross-section locations indicated in Figure 4. Solid black lines show 410-, 660-, and 1,000-km depth, respectively.

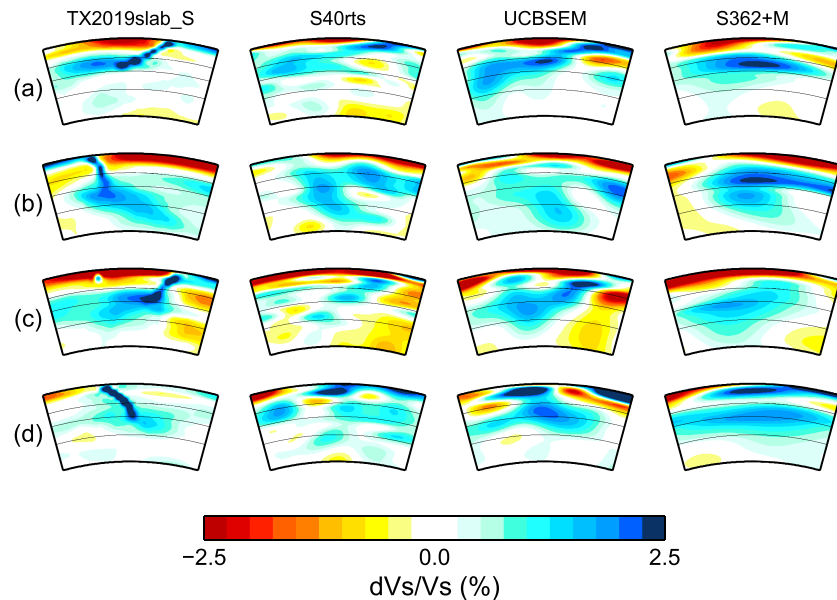


Figure 8. Comparison of cross sections across major subduction zones in representative S wave tomography models. Each column shows specific tomography models, including TX2019_slab (this study), S40rts (Ritsema et al., 2011), UCBSEM (French & Romanowicz, 2014), and S362+M (Moulik & Ekström, 2014). Each row corresponds to cross-section locations indicated in Figure 4. Solid black lines show 410-, 660-, and 1,000-km depth, respectively.

the S wave data. Our S wave model shows similar features as seen in our P wave model, including dipping, stagnant, and penetrated slabs (Figure S6). The other three S wave models, however, only show very long-wavelength fast velocity anomalies, which makes it challenging to identify the location and shape of subducting slabs. Also, the amplitude of the subducting slabs in our S wave model are mostly higher than 3%, which are again much higher than in the other models.

The S to P heterogeneity ratio, defined as

$$R_{V_S/V_P} = \frac{\partial \ln V_S}{\partial \ln V_P} \quad (4)$$

has been widely used as an important diagnostic parameter to determine the compositional state of the Earth's mantle, especially in the deeper mantle (e.g., Della Mora et al., 2011; Houser et al., 2008; Karato & Karki, 2001; Koelemeijer et al., 2016; Masters et al., 2000; Robertson & Woodhouse, 1996; Saltzer et al., 2001; Tesoniero et al., 2016). Several approaches have been used to calculate the S to P mantle heterogeneity ratio (see Tesoniero et al., 2016 for a summary). It has been shown that different approaches can lead to different heterogeneity ratios, even using the same tomography model (Koelemeijer et al., 2016). We used two methods to determine the 1-D S to P heterogeneity as a function a depth using our TX2019slab model (Figures 9 and S7). In the first method, a point to point division is computed except for regions where V_p or V_s variations are less than 0.1%. Regions that have opposite sign V_p and V_s anomalies, which contribute to about 5% of the volume of the mantle, were also excluded. The median values at each depth are chosen as the 1-D heterogeneity ratio. In the second method, we divided the RMS of the velocity variations for P and S at each depth after excluding small or opposite variations as in the first method (Figure 9). Throughout most of the mantle, the S to P ratio derived by RMS division is higher than by point to point division. A similar observation is seen in the comparison done by Koelemeijer et al. (2016) using tomography model KRDH16. This is due to the fact that the RMS value is more sensitive to outliers than the median value. The LLSVPs have large shear anomalies with smaller P anomalies and are the primary cause of the difference between the two methods in the deepest mantle. Even though the two methods described above lead to different 1-D S to P ratios, both S to P ratio models show similar trends.

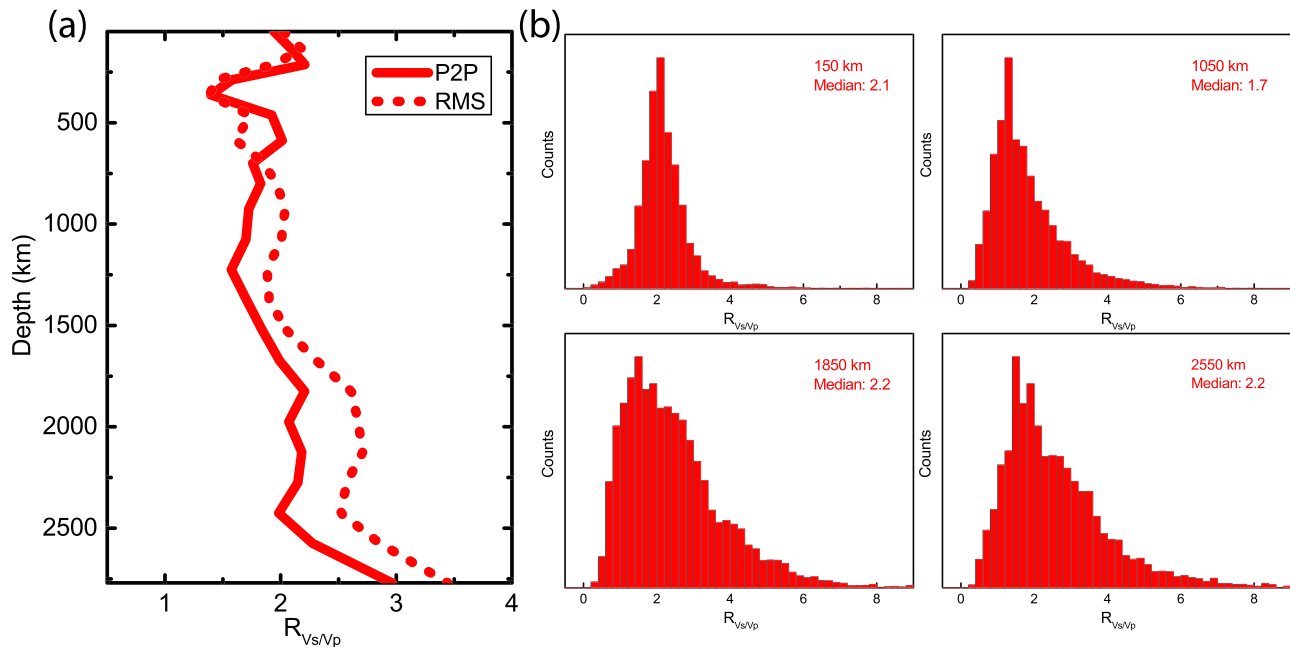


Figure 9. (a) S to P heterogeneity ratio derived using the TX2019slab model as a function of depth. Two S to P ratio profiles are derived by point to point (P2P) division and RMS value division, respectively. (b) Distribution of P2P division results at selected depths.

Lu and Grand (2016) showed that earthquake mislocation caused by subducting slabs could bias the tomography results in the lower mantle. This bias has the potential to further affect our estimation of the S to P ratio. To evaluate this effect, we also derived the S to P heterogeneity ratio for model TX2019 model using the two approaches described above (Figure 10). We find very little difference in the S to P heterogeneity ratio between the slab model and the model without starting slabs. We also calculated the point to point S to P ratio differences between the TX2019slab and TX2019 models and plot them in map view in Figure 11. The S to P ratio can differ by more than 0.5 between the models in specific regions. This is a significant difference since the lateral average S to P ratio in the lower mantle is between 1.5 and 3.5 in our model. Our analysis shows that the 1-D average of P to S heterogeneity ratio is unlikely to be significantly affected by the bias introduced by unmodeled subducting slabs. However, the bias may be quite large for the S to P heterogeneity ratio on a regional scale.

In the deeper mantle, our 1-D S to P heterogeneity ratio profiles show an increase with depth, which is consistent with most previous tomography studies (Antolik et al., 2003; Della Mora et al., 2011; Ishii & Tromp, 1999; Koelemeijer et al., 2016; Masters et al., 2000; Mosca et al., 2012; Resovsky & Trampert, 2003; Romanowicz, 2001; Su & Dziewonski, 1997; Tesoniero et al., 2016) (Figure 12). We followed Koelemeijer et al. (2016) and used the RMS division method for all the models in Figure 12. The S to P heterogeneity ratio profiles derived using body wave seismic data alone are plotted separately (Figure 12a) from results that also used normal model data (Figure 12b). Among these profiles, the $R_{Vs/Vp}$ range from about 1.5 to 4 throughout the lower mantle. The $R_{Vs/Vp}$ profiles vary more dramatically in the deep lower mantle than at shallower depths among the different models. In particular, most of the $R_{Vs/Vp}$ profiles agree with each other above 1,500-km depth. These models were produced using different data sets and different inversion strategies; therefore, the similarity indicates a convergence of $R_{Vs/Vp}$ estimations in this depth range. In the deep lower mantle, $R_{Vs/Vp}$ in KRHD16 (Koelemeijer et al., 2016) increases rapidly with depth and reaches ~ 4 near 2,450 km, then decreases again to the CMB. This feature is not seen in the other models. Most of the other models, including TX2019slab, show a gradual increasing $R_{Vs/Vp}$ with depth in this depth range. In contrast, there are several models have a small decrease above the CMB, including DBTNG11 (Della Mora et al., 2011), R01 (Romanowicz, 2001), TCB16 (Tesoniero et al., 2016), and SFBG10 (Simmons et al., 2010).

Figure 12c compares our $R_{Vs/Vp}$ in the lower mantle with predictions assuming that seismic heterogeneity is due to thermal variations alone. All the predicted $R_{Vs/Vp}$ profiles in Figure 12c assume a simple

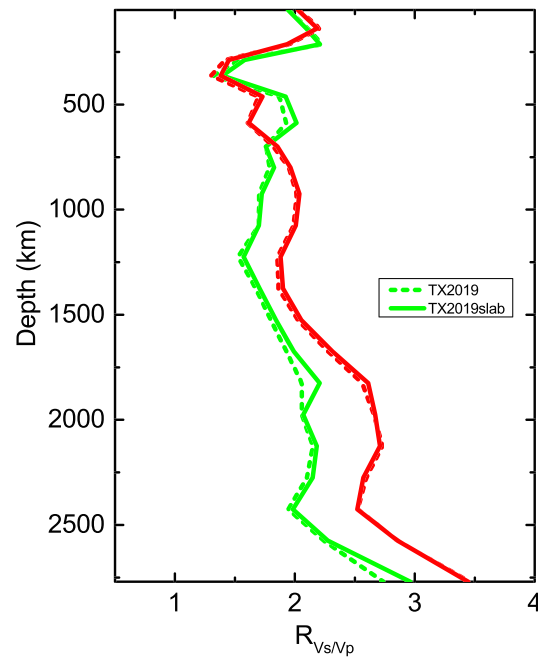


Figure 10. Comparison of S to P heterogeneity ratios using TX2019slab (solid lines) and TX2019 (dash lines). S to P ratio profiles are derived by point to point (P2P) division (green lines) and RMS value division (red lines), respectively.

“pyrolite” mineral assemblage model (e.g., Stixrude & Lithgow-Bertelloni, 2012) without invoking more complex proposed scenarios in the lower mantle such as spin transition effects (Lin et al., 2013; Wu & Wentzcovitch, 2014) or the phase transition from bridgmanite to post-perovskite (pPv; Murakami et al., 2004; Oganov & Ono, 2004; Tsuchiya et al., 2004). The estimate of R_{V_s/V_p} by Karato and Karki (2001) is lower than values we obtained using the RMS division method from about 1,500-km depth and below

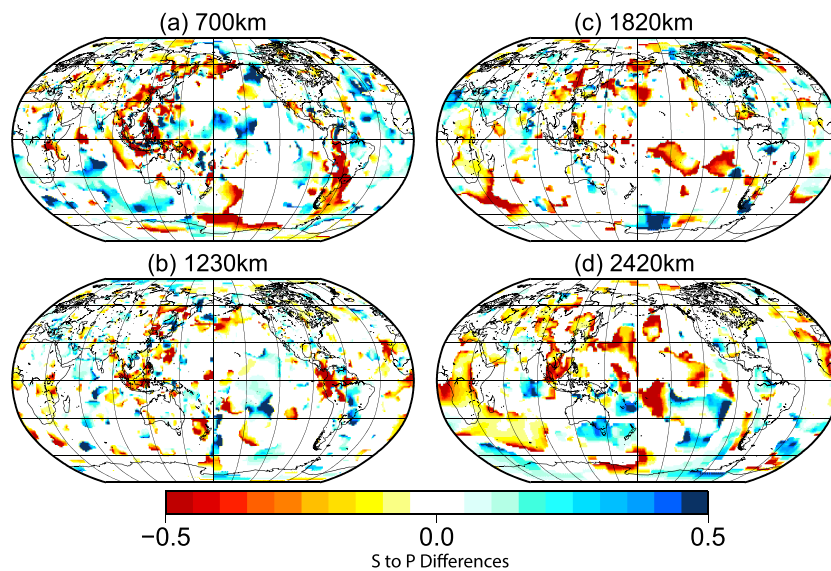


Figure 11. The difference in point to point S to P heterogeneity ratio between the TX2019slab and TX2019 models in map view at representative depths. The S to P heterogeneity ratio was calculated in each individual block. Although the 1-D average S to P heterogeneity ratio is not significantly different between these two models, the incorrect imaging of subducting slabs could bias the tomography results in the lower mantle in specific regions, as shown by high-amplitude regions in this figure.

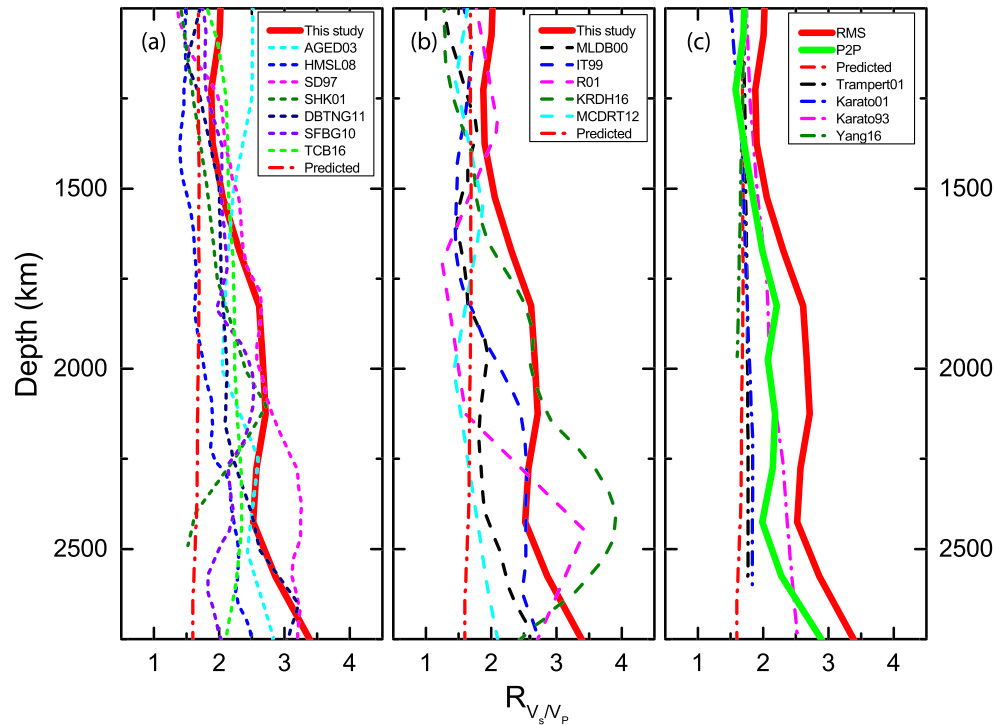


Figure 12. Comparison of S to P heterogeneity ratios in the lower mantle from (a) pure body wave seismic study, (b) normal mode data involved seismic study, and (c) mineral physics predictions assuming a thermal cause for heterogeneity in the lower mantle. Results in this study are shown using red solid (RMS division method) and green solid lines (point to point method). S to P heterogeneity ratio derived from mineral physics modeling from this study and used in the P and S joint inversion is also shown as a red dot dash line. (a) Results from previous pure body wave studies include AGED03 (Antolik et al., 2003), HMSL08 (Houser et al., 2008), SD97 (Su & Dziewonski, 1997), SHK01 (Saltzer et al., 2001), DBTNG11 (Della Mora et al., 2011), SFBG10 (Simmons et al., 2010), and TCB16 (Tesoniero et al., 2016). All the S to P heterogeneity ratios were obtained using the RMS value division method. (b) Results from models that used normal mode data include MLDB00 (Masters et al., 2000), IT99 (Ishii & Tromp, 1999), R01 (Romanowicz, 2001), KRDH16 (Koelemeijer et al., 2016), and MCDRT12 (Mosca et al., 2012). All the S to P heterogeneity ratios again were obtained using the RMS value division method. (c) Thermally induced S to P heterogeneity ratios derived from mineral physics modeling including the effect of anelasticity (Trampert et al., 2001; Karato, 1993; Karato & Karki, 2001; Yang et al., 2016) are shown in colored dot dash lines.

but is similar to values we derived using point to point division. However, the Karato and Karki (2001) estimates are significantly higher than other mineral physics predictions (Karato, 1993; Trampert et al., 2001; Yang et al., 2016) as well as ours. Two studies have argued that Karato and Karki (2001) overestimated the effect of anelasticity in the lower mantle, which would overpredict R_{V_s/V_p} since the temperature derivative of shear wave velocity is more sensitive to the anelasticity effect (Brodholt et al., 2007; Matas & Bukowski, 2007). If this is the case, our derived R_{V_s/V_p} implies factors other than simple thermal variations, starting from near 1,500-km depth, contribute to seismic heterogeneity. We also plotted the predicted R_{V_s/V_p} from mineral physics modeling in this study in Figures 12a and 12b. All of the seismically derived R_{V_s/V_p} profiles have higher values than mineral physics predictions in the deep lower mantle, which implies the existence of more complex thermal-chemical heterogeneities, although the amount and depth of these heterogeneities still vary among models and methods for estimating 1-D R_{V_s/V_p} .

Anelasticity in the Earth for P and S waves is quantified by quality factors Q_p and Q_s , respectively. The quality factor Q due to viscoelastic relaxation can be written as (Karato, 1993)

$$Q(\omega, T) = Q_0 \omega^\alpha \exp\left(\frac{\alpha H^*}{RT}\right) \quad (5)$$

where ω is the seismic frequency, α is the exponent describing the frequency dependence of the attenuation, T is the temperature, R is the gas constant, H^* is the activation enthalpy, and Q_0 is a normalization constant that can be constrained using seismically observed attenuation. Assuming that bulk attenuation is

negligible, the relationship between elastic (“*el*”) and anelastic (“*anel*”) values of R_{V_s/V_p} can be given by (Matas & Bukowski, 2007)

$$R_{V_s/V_p}^{anel} = R_{V_s/V_p}^{el} + \frac{A_P}{V_{P,T} + A_P} \left(\frac{3V_P^2}{4V_S^2} - R_{V_s/V_p}^{el} \right) \quad (6)$$

where

$$A_P = -\frac{\alpha H^* \cot(\alpha\pi/2)}{2Q_P RT^2} \quad (7)$$

$$V_{P,T} = \frac{\partial \ln V_P^{el}}{\partial T} \quad (8)$$

The measurements of several critical anelasticity-related parameters, including H^* and α , still vary a lot among different studies (see Brodholt et al. (2007) and Matas and Bukowski (2007) for summaries). Therefore, the predicted R_{V_s/V_p} from mineral physics after taking anelasticity into account may contain significant uncertainties. In Figure 13, we evaluated the potential effect of anelasticity on predicted R_{V_s/V_p} to check whether the uncertainty in anelasticity could explain the apparent discrepancies between seismic observed and mineral physics predicted R_{V_s/V_p} in the deep lower mantle (Figure 12c). To make the comparison more diagnostic, we plotted the variation of R_{V_s/V_p} as a function of S velocity perturbation at selected depths instead of using a 1-D profile. We varied the anelasticity-related parameters within their possible ranges to fully explore the possible anelasticity effect. Figures 13b (and 13c only show estimates at 2,000-km depth but we found similar results at all other depths. According to our test, when the anelasticity effect is strong, mineral physics predicted R_{V_s/V_p} becomes larger, but the amount of variation is limited. For example, the maximum R_{V_s/V_p} is ~ 2.5 at 2,000-km depth, which is comparable to our observed 1-D R_{V_s/V_p} in TX2019slab (Figure 12). But this maximum value requires the combination of extreme values for multiple parameters (i.e., $H^* = 800$ kJ/mol, $\alpha = 0.4$), that Brodholt et al. (2007) claim unlikely. For better visualization, we binned and averaged seismically derived R_{V_s/V_p} based on a 0.2% S velocity perturbation interval and applied a moving average filter in Figure 13a for comparison. At all selected depths, the seismically derived R_{V_s/V_p} profiles show “ V ” shapes: R_{V_s/V_p} values increase with increasing S wave perturbation, both in the positive and negative directions. The R_{V_s/V_p} for large S wave perturbation regions (larger than 1% for example) can easily be over 2.8 and even reach 5. Tesoniero et al. (2016) has shown that the “ V ” shape is a common feature in all the tomography models they tested and argued that the V shape could be a result of errors in seismic tomography. The effect of small errors on R_{V_s/V_p} values can be amplified when the true velocity perturbation is small because of the division between S and P wave anomalies (see Tesoniero et al. (2016) for more discussion). If Tesoniero et al. (2016) are correct, it means that the R_{V_s/V_p} in the large S wave perturbation regions are more reliable than in the small-velocity perturbation regions. In other words, the actual R_{V_s/V_p} could be higher than our 1-D seismic observation in Figure 12, which means that anelasticity effects alone cannot explain the observed R_{V_s/V_p} assuming that heterogeneity is due to thermal effects in a chemically homogeneous mantle. More complex thermal-chemical structures are needed to explain our seismic observed R_{V_s/V_p} in the deep lower mantle.

An interesting feature in our S to P heterogeneity profile is that the ratio increases starting from 1,400-km depth and reaches a local maximum around 1,800-km depth, stays relatively constant to 2,100-km depth, then decreases before a large jump near the CMB. Both our derived S to P heterogeneity ratios have this pattern, although the S to P ratio derived by RMS division shows this feature more clearly. Model SD97 (Su & Dziewonski, 1997) and KR16 (Koelemeijer et al., 2016) show a similar trend above 2,100-km depth but R_{V_s/V_p} continues to increase with depth below 2,100 km. Several other models have similar peaks but at deeper depth, including SFBG10 (Simmons et al., 2010), SHK01 (Saltzer et al., 2001), IT99 (Ishii & Tromp, 1999), (Romanowicz, 2001), and MLDB00 (Masters et al., 2000). Wu and Wentzcovitch (2014) reported that the P wave velocity of pyrolitic lower mantle becomes insensitive to temperature variations due to the spin transition between $\sim 1,400$ - and $\sim 2,100$ -km depth. This would increase the S to P heterogeneity there even if variations were solely due to thermal effects. Thus, the abnormal R_{V_s/V_p} we observe between 1,400 and 2,100 km

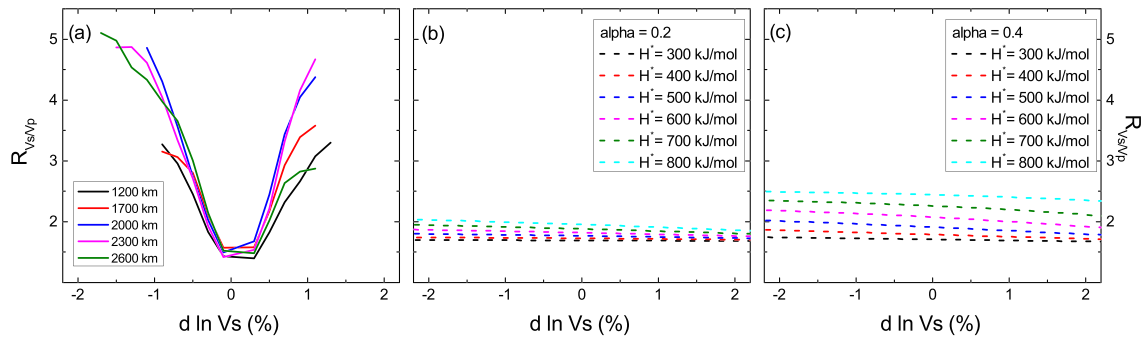


Figure 13. Comparison of seismically observed S to P heterogeneity ratios versus S velocity perturbations and mineral physics predictions assuming different anelasticity parameters. (a) Results calculated for TX2019slab model at selected depths. The average scaling factors are calculated for each 0.2% velocity perturbation interval. A three-point moving-average filter was applied before plotting for better visualization. (b) Mineral physics predictions at 2,000-km depth with varying $H^{\bar{}}$. α is fixed at 0.2 and Q_0 is derived following Matas and Bukowinski (2007) method assuming average lateral temperature variation $dT/T = 0.4$ and seismic observed quality factor $Q_s = 350$. (c) Similar as (b) but α is fixed at 0.4.

may partially be due to the spin transition in a mantle with heterogeneity dominated by temperature variations. In Figure 14 we compare the predicted R_{V_s/V_p} from Wu and Wentzcovitch (2014) to our results. Our result matches the mineral physics prediction for an aggregate consisting of 5 wt % ferropicclase ($Mg_{0.92}Fe_{0.08}SiO_3$) and the rest bridgmanite the best, which generally agrees with a bridgmanite-enriched mantle model proposed by Murakami et al. (2012). However, the modeling result of Wu and Wentzcovitch (2014) may oversimplify the effect of the spin transition in the mantle since it does not consider several critical effects such as iron-partitioning variations crossing the spin transition (e.g.,

Kobayashi et al., 2005; Lin et al., 2013), and the spin transition in Fe-bearing bridgmanite (e.g., Chantel et al., 2012; Fu et al., 2018). We leave to further work a more detailed analysis of the effect of the spin transition on the S to P heterogeneity ratio.

Karato and Karki (2001) claim that R_{V_s/V_p} cannot exceed 2.7 for an iso-chemical deep lower mantle. Our model, as well as several other models shown in Figure 12, shows the bottom 200 km of the mantle to have heterogeneity ratios well above 2.7. One major limitation of the mineral physics predictions we use is that they did not consider potential phase transitions occurring in the lower mantle. Bridgmanite could transform to pPv in the deepest ~400-km mantle (Murakami et al., 2004; Oganov & Ono, 2004; Tsuchiya et al., 2004). Compared with bridgmanite, pPv has similar P velocity and higher S velocity (Tsuchiya et al., 2004; Wookey et al., 2005). Wentzcovitch et al. (2006) reported a very large R_{V_s/V_p} (>6) caused by the pPv transition along their predicted phase boundary (Figure 14). Lateral variation in phase abundances can explain the high R_{V_s/V_p} we found in our model in the bottom few hundred kilometers of the mantle. The amplitude differences between the results of Wentzcovitch et al. (2006) and seismic observations could be caused by uncertainties in the mineral physics modeling, such as the pressure and temperature sensitivity of the bridgmanite to pPv phase transition (Cobden et al., 2015), and the possible presence of subducted MORB or iron at the lowest mantle (Grocholski et al., 2012; Tateno et al., 2007).

Figure 15 shows radial depth profiles of the correlation coefficient (CC) between P and S wave perturbations, the RMS velocity anomalies for P and S , and the CC between bulk sound and shear speed perturbations. P and S velocity heterogeneities are highly correlated throughout the mantle in our model (Figure 15a). The RMS amplitude of S wave

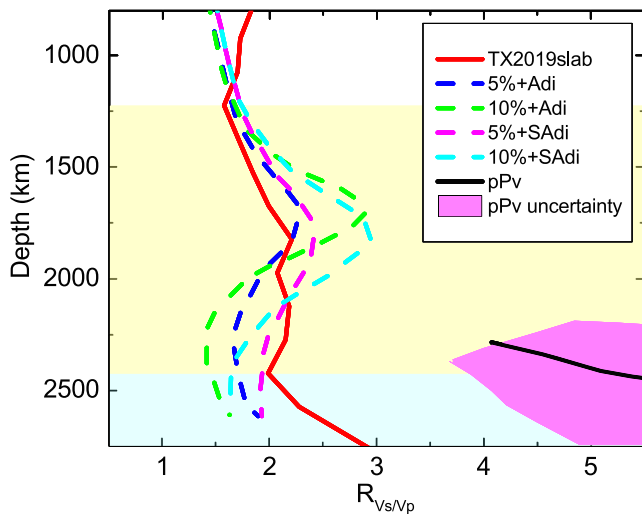


Figure 14. Comparison of the S to P heterogeneity ratios in the TX2019slab model and mineral physics predictions including the effects of the spin transition and the pPv phase transition. The mineral physics predictions accounting for the spin transition (dash lines) are adopted from Wu and Wentzcovitch (2014). Thermally induced S to P heterogeneity ratios in aggregates along adiabatic (Adi) and superadiabatic (SAdi) geotherms are shown. Aggregates consist of 5 or 10 wt % ferropicclase ($Mg_{0.92}Fe_{0.08}SiO_3$) and bridgmanite. The predicted S to P heterogeneity ratio due to the bridgmanite to pPv transition along the phase boundary (solid black line) is shown with uncertainty (shaded purple area) from Wentzcovitch et al. (2006). The light yellow background color indicates the proposed depth range for the spin transition effect and light background below shows the depths where the pPv phase transition could occur.

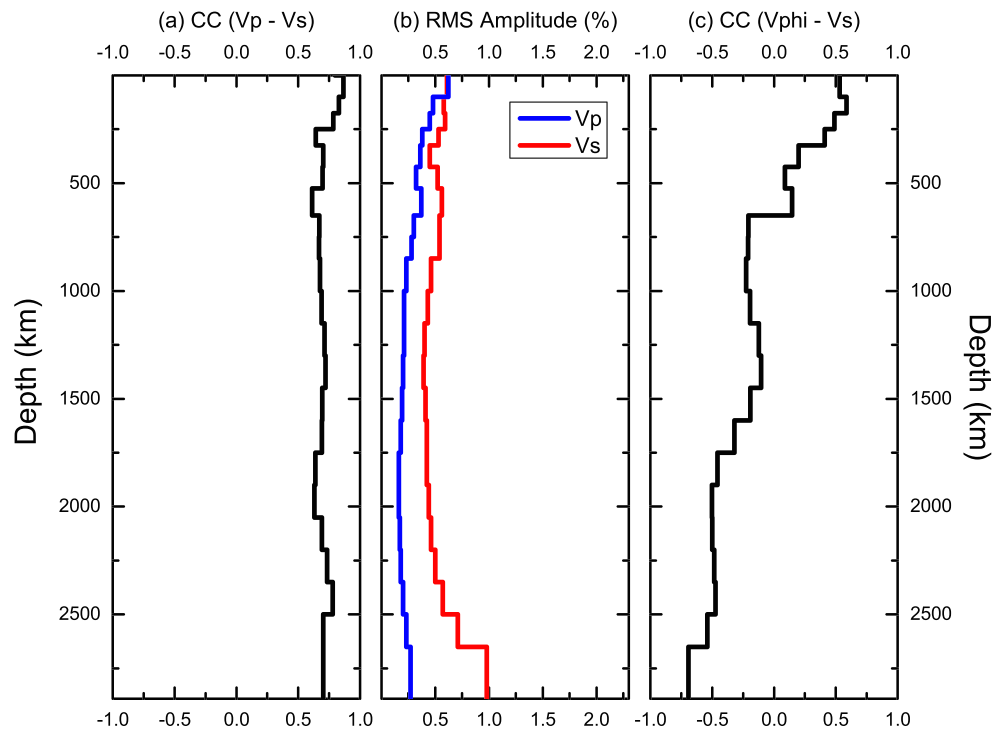


Figure 15. Depth profiles calculated for the TX2019slab model. (a) Correlation between P and S wave heterogeneities. (b) RMS amplitude of P and S wave anomalies. (c) Correlation between bulk and shear wave anomalies. Bulk and shear speeds become decorrelated in the shallow lower mantle (~ 700 - to $\sim 1,500$ -km depth) and anticorrelated below 1,500-km depth.

perturbations is higher than P waves at all depths, which agrees with previous studies (e.g., Koelemeijer et al., 2016; Simmons et al., 2010; Figure 15b). The depth profile of the correlation between bulk sound and shear speeds shows a more complex variation (Figure 15c). In the upper mantle, the bulk sound speed correlates well with shear speed. In the shallow and mid-lower mantle, the bulk sound speed anomalies are almost decorrelated with S wave anomalies. Sound and shear speeds become anticorrelated below $\sim 1,500$ -km depth. Similar anticorrelation of sound and shear speeds in the deep lower mantle has been reported in several other tomography studies (e.g., Koelemeijer et al., 2016; Masters et al., 2000; Simmons et al., 2010; Su & Dziewonski, 1997). The anticorrelation between shear wave and bulk sound speed anomalies has been used to argue for chemical variations in the deep mantle. However, previous investigations have shown that both the spin transition effect (Wu & Wentzcovitch, 2014) and the phase transition from bridgmanite to pPv (Wookey et al., 2005) can cause anticorrelation between sound and shear speeds in the deep mantle. Thus, the anticorrelation we observe in our model could still be explained by thermal effects alone for an isochemical mantle, although it likely requires a strong effect of the spin transition.

It is still challenging to draw concrete conclusions about the thermal-chemical structure in the lower mantle using P - S tomography results alone. Although the observed R_{V_s/V_p} is higher in the deep mantle than predicted by simple calculations assuming that heterogeneity is due to thermal effects alone, the effects of the spin transition, phase changes, and anelasticity can increase the scaling beyond what has been considered in the past for an isochemical mantle. Detailed evaluation of several critical topics are still lacking to definitively rule out a thermal explanation for mantle heterogeneity. These include the effect of iron-partitioning variations crossing the spin transition (e.g., Kobayashi et al., 2005; Lin et al., 2013), the spin transition in Fe-bearing bridgmanite (e.g., Chantel et al., 2012; Fu et al., 2018), the pressure and temperature sensitivity of the bridgmanite to pPv phase transition (Cobden et al., 2015), and the vertical smearing effect in tomography models.

5. Conclusions

In this study, we produce a new P and S global tomography model. The most significant improvement in our inversion, relative to our past work, is that we include a priori 3-D subducting slabs in our starting model and inverted for velocity and source parameters simultaneously. Both of our P and S wave models feature higher-amplitude subducting slabs compared with previous global tomography results, which better matches observations using other approaches. We also calculated the S to P heterogeneity ratio using our model. Although the 1-D S to P heterogeneity ratio is not significantly different using models with starting slabs relative to models without, we found that the incorrect imaging of subducting slabs could bias the tomography results in the lower mantle in specific regions. Our derived S to P ratio features a broad peak at around 1,800- to 2,100-km depth, which is consistent with mineral physics predictions of the spin transition effect. The high S to P ratio right above CMB can be due to bridgmanite to pPv phase change. However, our observations alone cannot rule out the possibility of the existence of chemical heterogeneities in the deep lower mantle.

Acknowledgments

The TX2019slab model is available at IRIS EMC website (<http://ds.iris.edu/ds/products/emc-earthmodels/>). We thank ISC (International Seismological Centre, <http://www.isc.ac.uk/isc-ehb/>), IRIS DMC (Incorporated Research Institutions for Seismology, Data Management Center, <https://ds.iris.edu/ds/nodes/dmc/>), ORFEUS (Observations & Research Facilities for European Seismology, <https://www.orfeus-eu.org/>), NECDC (Northern California Earthquake Data Center, <http://ncedc.org/>), F-net (F-net Broadband Seismograph Network, <http://www.fnet.bosai.go.jp/>), and CNSN (Canadian National Seismic Network, <http://www.earthquakescanada.nrcan.gc.ca/stdon/CNDC/>) for providing seismic data used in this study. We thank Georg Stadler, Michael Gurnis, and Ellen Syracuse for providing thermal slab model. We also thank Nathan Simmons, Alessandro Forte, Jung-Fu Lin, Thorsten Becker, and Suyu Fu for the valuable discussions. This research was supported by National Science Foundation (NSF) grants EAR-1648770 and EAR-1648817 and by the Jackson School of Geosciences at the University of Texas at Austin.

References

- Amaru, M. L. (2007). Global travel time tomography with 3-D reference model (Doctoral dissertation). Utrecht, Netherlands: Utrecht University.
- Antolik, M., Gu, Y. J., Ekström, G., & Dziewonski, A. M. (2003). J362D28: a new joint model of compressional and shear velocity in the Earth's mantle. *Geophysical Journal International*, *153*(2), 443–466.
- Billen, M. I. (2008). Modeling the dynamics of subducting slabs. *Annual Review Earth Planetary Sciences*, *36*, 325–356.
- Bonnardot, M. A., Régnier, M., Christova, C., Ruellan, E., & Tric, E. (2009). Seismological evidence for a slab detachment in the Tonga subduction zone. *Tectonophysics*, *464*(1), 84–99. <https://doi.org/10.1016/j.tecto.2008.10.011>
- Brodholt, J. P., Helffrich, G., & Trampert, J. (2007). Chemical versus thermal heterogeneity in the lower mantle: The most likely role of anelasticity. *Earth and Planetary Science Letters*, *262*(3), 429–437. <https://doi.org/10.1016/j.epsl.2007.07.054>
- Brudzinski, M. R., & Chen, W.-P. (2005). Earthquakes and strain in subhorizontal slabs. *Journal of Geophysical Research*, *110*(B8), B08303. <https://doi.org/10.1029/2004JB003470>
- Chantel, J., Frost, D. J., McCammon, C. A., Jing, Z., & Wang, Y. (2012). Acoustic velocities of pure and iron-bearing magnesium silicate perovskite measured to 25 GPa and 1200 K. *Geophysical Research Letters*, *39*, L19307. <https://doi.org/10.1029/2012GL053075>
- Chen, M., Tromp, J., Helmberger, D., & Kanamori, H. (2007). Waveform modeling of the slab beneath Japan. *Journal of Geophysical Research*, *112*, B02305. <https://doi.org/10.1029/2006JB004394>
- Cobden, L., Thomas, C., & Trampert, J. (2015). Seismic Detection of Post-perovskite Inside the Earth. In A. Khan, & F. Deschamps (Eds.), *The Earth's Heterogeneous Mantle* (pp. 391–440). Switzerland: Springer.
- Creager, K. C., & Jordan, T. H. (1984). Slab penetration into the lower mantle. *Journal of Geophysical Research*, *89*, 3031–3049. <https://doi.org/10.1029/JB089iB05p03031>
- Della Mora, S., Boschi, L., Tackley, P., Nakagawa, T., & Giardini, D. (2011). Low seismic resolution cannot explain S/P decorrelation in the lower mantle. *Geophysical Research Letters*, *38*, L12303. <https://doi.org/10.1029/2011GL047559>
- Deschamps, F., Trampert, J., & Snieder, R. (2002). Anomalies of temperature and iron in the uppermost mantle inferred from gravity data and tomographic models. *Physics of the Earth and Planetary Interiors*, *129*(3), 245–264. [https://doi.org/10.1016/S0031-9201\(01\)00294-1](https://doi.org/10.1016/S0031-9201(01)00294-1)
- Ding, X. Y., & Grand, S. P. (1994). Seismic structure of the deep Kurile subduction zone. *Journal of Geophysical Research*, *99*(B12), 23,767–23,786. <https://doi.org/10.1029/94JB02130>
- Engdahl, E. R., van der Hilst, R. D., & Buland, R. (1998). Global teleseismic earthquake relocation with improved travel times and procedures for depth determination. *Bulletin of the Seismological Society of America*, *88*(3), 722–743.
- Forte, A. M., & Perry, H. C. (2000). Geodynamic evidence for a chemically depleted continental tectosphere. *Science*, *290*(5498), 1940–1944. <https://doi.org/10.1126/science.290.5498.1940>
- French, S. W., & Romanowicz, B. A. (2014). Whole-mantle radially anisotropic shear velocity structure from spectral-element waveform tomography. *Geophysical Journal International*, *199*(3), 1303–1327. <https://doi.org/10.1093/gji/ggu334>
- Fu, S., Yang, J., Zhang, Y., Okuchi, T., McCammon, C., Kim, H.-I., et al. (2018). Abnormal elasticity of Fe-bearing bridgmanite in the Earth's lower mantle. *Geophysical Research Letters*, *45*(10), 4725–4732. <https://doi.org/10.1029/2018GL077764>
- Fukao, Y., & Obayashi, M. (2013). Subducted slabs stagnant above, penetrating through, and trapped below the 660 km discontinuity. *Journal of Geophysical Research: Solid Earth*, *118*, 5920–5938. <https://doi.org/10.1002/2013JB010466>
- Gaherty, J. B., Lay, T., & Vidale, J. E. (1991). Investigation of deep slab structure using long-period S waves. *Journal of Geophysical Research*, *96*(B10), 16349–16367. <https://doi.org/10.1029/91JB01483>
- Garnero, E. J., McNamara, A. K., & Shim, S.-H. (2016). Continent-sized anomalous zones with low seismic velocity at the base of Earth's mantle. *Nature Geoscience*, *9*, 481–489. <https://doi.org/10.1038/ngeo2733>
- Grand, S. P. (1994). Mantle shear structure beneath the Americas and surrounding oceans. *Journal of Geophysical Research*, *99*, 11,591–11,621. <https://doi.org/10.1029/94JB00042>
- Grand, S. P. (2002). Mantle shear-wave tomography and the fate of subducted slabs. *Philosophical Transactions of the Royal Society of London A: Mathematical, Physical and Engineering Sciences*, *360*(1800), 2475–2491.
- Grand, S. P., & Helmberger, D. V. (1984). Upper mantle shear structure of North America. *Geophysical Journal International*, *76*(2), 399–438. <https://doi.org/10.1111/j.1365-246X.1984.tb05053.x>
- Grocholski, B., Catalli, K., Shim, S.-H., & Prakapenka, V. (2012). Mineralogical effects on the detectability of the postperovskite boundary. *Proceedings of the National Academy of Science*, *109*(7), 2275–2279.
- Hayes, G. P., Wald, D. J., & Johnson, R. L. (2012). Slab1.0: A three-dimensional model of global subduction zone geometries. *Journal of Geophysical Research*, *117*(B1), B01302. <https://doi.org/10.1029/2011JB008524>
- Houser, C., Masters, G., Shearer, P., & Laske, G. (2008). Shear and compressional velocity models of the mantle from cluster analysis of long-period waveforms. *Geophysical Journal International*, *174*(1), 195–212. <https://doi.org/10.1111/j.1365-246X.2008.03763.x>

- Ishii, M., & Tromp, J. (1999). Normal-mode and free-air gravity constraints on lateral variations in velocity and density of Earth's mantle. *Science*, 285(5431), 1231–1236. <https://doi.org/10.1126/science.285.5431.1231>
- Karato, S.-i. (1993). Importance of anelasticity in the interpretation of seismic tomography. *Geophysical Research Letters*, 20(15), 1623–1626. <https://doi.org/10.1029/93GL01767>
- Karato, S.-i., & Karki, B. B. (2001). Origin of lateral variation of seismic wave velocities and density in the deep mantle. *Journal of Geophysical Research*, 106(B10), 21,771–21,783. <https://doi.org/10.1029/2001JB000214>
- Kawakatsu, H., & Yoshioka, S. (2011). Metastable olivine wedge and deep dry cold slab beneath southwest Japan. *Earth and Planetary Science Letters*, 303(1), 1–10. <https://doi.org/10.1016/j.epsl.2011.01.008>
- Kellogg, L. H., Hager, B. H., & van der Hilst, R. D. (1999). Compositional Stratification in the Deep Mantle. *Science*, 283(5409), 1881–1884. <https://doi.org/10.1126/science.283.5409.1881>
- Kennett, B. L. N., Engdahl, E. R., & Buland, R. (1995). Constraints on seismic velocities in the Earth from traveltimes. *Geophysical Journal International*, 122(1), 108–124. <https://doi.org/10.1111/j.1365-246X.1995.tb03540.x>
- Kobayashi, Y., Kondo, T., Ohtani, E., Hirao, N., Miyajima, N., Yagi, T., et al. (2005). Fe-Mg partitioning between (Mg, Fe)SiO₃ post-perovskite, perovskite, and magnesio-wüstite in the Earth's lower mantle. *Geophysical Research Letters*, 32, L19301. <https://doi.org/10.1029/2005GL023257>
- Koelemeijer, P., Ritsema, J., Deuss, A., & van Heijst, H. J. (2016). SP12RTS: a degree-12 model of shear- and compressional-wave velocity for Earth's mantle. *Geophysical Journal International*, 204(2), 1024–1039. <https://doi.org/10.1093/gji/ggv481>
- Komatitsch, D., & Tromp, J. (2002a). Spectral-element simulations of global seismic wave propagation—I. Validation. *Geophysical Journal International*, 149(2), 390–412.
- Komatitsch, D., & Tromp, J. (2002b). Spectral-element simulations of global seismic wave propagation—II. Three-dimensional models, oceans, rotation and self-gravitation. *Geophysical Journal International*, 150(1), 303–318.
- Kustowski, B., Ekström, G., & Dziewieński, A. (2008). Anisotropic shear-wave velocity structure of the Earth's mantle: A global model. *Journal of Geophysical Research*, 113, B06306. <https://doi.org/10.1029/2007JB005169>
- Lai, H., Garnero, E. J., Grand, S. P., Porritt, R. W., & Becker, T. W. (2019). Global travel time dataset from adaptive empirical wavelet construction. *Geochemistry, Geophysics, Geosystems*, 20. <https://doi.org/10.1029/2018GC007905>
- Laske, G., Masters, G., Ma, Z., & Pasyanos, M. (2013). Update on CRUST1.0-A 1-degree global model of Earth's crust. Paper presented at EGU General Assembly, Vienna, Austria.
- Lee, C. T. (2003). Compositional variation of density and seismic velocities in natural peridotites at STP conditions: Implications for seismic imaging of compositional heterogeneities in the upper mantle. *Journal of Geophysical Research*, 108(B9), 2441, ECV 6-1-6-20. <https://doi.org/10.1029/2003JB002413>
- Li, C., van der Hilst, R. D., Engdahl, E. R., & Burdick, S. (2008). A new global model for P wave speed variations in Earth's mantle. *Geochemistry, Geophysics, Geosystems*, 9, Q05018. <https://doi.org/10.1029/2007GC001806>
- Lin, J.-F., Speziale, S., Mao, Z., & Marquardt, H. (2013). Effects of the electronic spin transitions of iron in lower mantle minerals: implications for deep mantle geophysics and geochemistry. *Reviews of Geophysics*, 51, 244–275. <https://doi.org/10.1002/rog.20010>
- Lu, C., & Grand, S. P. (2016). The effect of subducting slabs in global shear wave tomography. *Geophysical Journal International*, 205(2), 1074–1085. <https://doi.org/10.1093/gji/ggw072>
- Masters, G., Laske, G., Bolton, H., & Dziewieński, A. (2000). The Relative Behavior of Shear Velocity, Bulk Sound Speed, and Compressional Velocity in the Mantle: Implications for Chemical and Thermal Structure. In S. i. Karato, A. Forte, R. Liebermann, G. Masters, & L. Stixrude (Eds.), *Earth's Deep Interior: Mineral Physics and Tomography From the Atomic to the Global Scale*, *Geophysical Monograph Series* (Vol. 117, pp. 63–87). Washington, DC: American Geophysical Union.
- Matas, J., & Bukowinski, M. S. T. (2007). On the anelastic contribution to the temperature dependence of lower mantle seismic velocities. *Earth and Planetary Science Letters*, 259(1), 51–65. <https://doi.org/10.1016/j.epsl.2007.04.028>
- Mosca, I., Cobden, L., Deuss, A., Ritsema, J., & Trampert, J. (2012). Seismic and mineralogical structures of the lower mantle from probabilistic tomography. *Journal of Geophysical Research*, 117, B06304. <https://doi.org/10.1029/2011JB008851>
- Moulik, P., & Ekström, G. (2014). An anisotropic shear velocity model of the Earth's mantle using normal modes, body waves, surface waves and long-period waveforms. *Geophysical Journal International*, 199(3), 1713–1738.
- Murakami, M., Hirose, K., Kawamura, K., Sata, N., & Ohishi, Y. (2004). Post-perovskite phase transition in MgSiO₃. *Science*, 304(5672), 855–858. <https://doi.org/10.1126/science.1095932>
- Murakami, M., Ohishi, Y., Hirao, N., & Hirose, K. (2012). A perovskitic lower mantle inferred from high-pressure, high-temperature sound velocity data. *Nature*, 485, 90–94.
- Obayashi, M., Yoshimitsu, J., Nolet, G., Fukao, Y., Shiobara, H., Sugioka, H., et al. (2013). Finite frequency whole mantle P wave tomography: Improvement of subducted slab images. *Geophysical Research Letters*, 40, 5652–5657. <https://doi.org/10.1002/2013GL057401>
- Oganov, A. R., & Ono, S. (2004). Theoretical and experimental evidence for a post-perovskite phase of MgSiO₃ in Earth's D'' layer. *Nature*, 430(6998), 445–448.
- Panning, M., & Romanowicz, B. (2006). A three-dimensional radially anisotropic model of shear velocity in the whole mantle. *Geophysical Journal International*, 167(1), 361–379. <https://doi.org/10.1111/j.1365-246X.2006.03100.x>
- Perry, H. K. C., Forte, A. M., & Eaton, D. W. S. (2003). Upper-mantle thermochemical structure below North America from seismic-geodynamic flow models. *Geophysical Journal International*, 154(2), 279–299. <https://doi.org/10.1046/j.1365-246X.2003.01961.x>
- Resovsky, J., & Trampert, J. (2003). Using probabilistic seismic tomography to test mantle velocity-density relationships. *Earth and Planetary Science Letters*, 215(1), 121–134. [https://doi.org/10.1016/S0012-821X\(03\)00436-9](https://doi.org/10.1016/S0012-821X(03)00436-9)
- Richards, S., Holm, R., & Barber, G. (2011). When slabs collide: A tectonic assessment of deep earthquakes in the Tonga-Vanuatu region. *Geology*, 39(8), 787–790. <https://doi.org/10.1130/G31937.1>
- Ritsema, J., Deuss, A., van Heijst, H. J., & Woodhouse, J. H. (2011). S40RTS: a degree-40 shear-velocity model for the mantle from new Rayleigh wave dispersion, teleseismic traveltime and normal-mode splitting function measurements. *Geophysical Journal International*, 184, 1223–1236. <https://doi.org/10.1111/j.1365-246X.2010.04884.x>
- Robertson, G., & Woodhouse, J. (1996). Ratio of relative S to P velocity heterogeneity in the lower mantle. *Journal of Geophysical Research*, 101(B9), 20041–20052. <https://doi.org/10.1029/96JB01905>
- Romanowicz, B. (2001). Can we resolve 3D density heterogeneity in the lower mantle? *Geophysical Research Letters*, 28(6), 1107–1110. <https://doi.org/10.1029/2000GL012278>
- Saltzer, R. L., van der Hilst, R. D., & Karason, H. (2001). Comparing P and S wave heterogeneity in the mantle. *Geophysical Research Letters*, 28(7), 1335–1338. <https://doi.org/10.1029/2000GL012339>

- Simmons, N. A., Forte, A. M., Boschi, L., & Grand, S. P. (2010). GyPSuM: A joint tomographic model of mantle density and seismic wave speeds. *Journal of Geophysical Research*, *115*, B12310. <https://doi.org/10.1029/2010JB007631>
- Simmons, N. A., Myers, S. C., Johannesson, G., & Matzel, E. (2012). LLNL-G3Dv3: Global *P* wave tomography model for improved regional and teleseismic travel time prediction. *Journal of Geophysical Research*, *117*, B10302. <https://doi.org/10.1029/2012JB009525>
- Sleep, N. H. (1973). Teleseismic *P*-wave transmission through slabs. *Bulletin of the Seismological Society of America*, *63*(4), 1349–1373.
- Stadler, G., Gurnis, M., Burstedde, C., Wilcox, L. C., Alisic, L., & Ghattas, O. (2010). The Dynamics of Plate Tectonics and Mantle Flow: From Local to Global Scales. *Science*, *329*(5995), 1033–1038. <https://doi.org/10.1126/science.1191223>
- Stixrude, L., & Lithgow-Bertelloni, C. (2012). Geophysics of Chemical Heterogeneity in the Mantle. *Annual Review of Earth and Planetary Sciences*, *40*(1), 569–595. <https://doi.org/10.1146/annurev.earth.36.031207.124244>
- Su, W.-j., & Dziewonski, A. M. (1997). Simultaneous inversion for 3-D variations in shear and bulk velocity in the mantle. *Physics of the Earth and Planetary Interiors*, *100*(1), 135–156. [https://doi.org/10.1016/S0031-9201\(96\)03236-0](https://doi.org/10.1016/S0031-9201(96)03236-0)
- Syracuse, E. M., van Keken, P. E., & Abers, G. A. (2010). The global range of subduction zone thermal models. *Physics of the Earth and Planetary Interiors*, *183*(1), 73–90. <https://doi.org/10.1016/j.pepi.2010.02.004>
- Tao, K., Grand, S. P., & Niu, F. (2018). Seismic structure of the upper mantle beneath eastern Asia from full waveform seismic tomography. *Geochemistry, Geophysics, Geosystems*, *19*, 2732–2763. <https://doi.org/10.1029/2018GC007460>
- Tateno, S., Hirose, K., Sata, N., & Ohishi, Y. (2007). Solubility of FeO in (Mg, Fe)SiO₃ perovskite and the post-perovskite phase transition. *Physics of the Earth and Planetary Interiors*, *160*(3), 319–325.
- Tesoniero, A., Cammarano, F., & Boschi, L. (2016). S-to-P heterogeneity ratio in the lower mantle and thermo-chemical implications. *Geochemistry, Geophysics, Geosystems*, *17*, 2522–2538. <https://doi.org/10.1002/2016GC006293>
- Trampert, J., Vacher, P., & Vlaar, N. (2001). Sensitivities of seismic velocities to temperature, pressure and composition in the lower mantle. *Physics of the Earth and Planetary Interiors*, *124*(3), 255–267. [https://doi.org/10.1016/S0031-9201\(01\)00201-1](https://doi.org/10.1016/S0031-9201(01)00201-1)
- Tsuchiya, T., Tsuchiya, J., Umemoto, K., & Wentzcovitch, R. M. (2004). Phase transition in MgSiO₃ perovskite in the earth's lower mantle. *Earth and Planetary Science Letters*, *224*(3–4), 241–248.
- van Keken, P. E., Hacker, B. R., Syracuse, E. M., & Abers, G. A. (2011). Subduction factory: 4. Depth-dependent flux of H₂O from subducting slabs worldwide. *Journal of Geophysical Research*, *116*, B01401. <https://doi.org/10.1029/2010JB007922>
- Vidale, J. E. (1987). Waveform effects of a high-velocity, subducted slab. *Geophysical Research Letters*, *14*(5), 542–545. <https://doi.org/10.1029/GL014i005p00542>
- Wang, T., Revenaugh, J., & Song, X. (2014). Two-dimensional/three-dimensional waveform modeling of subducting slab and transition zone beneath Northeast Asia. *Journal of Geophysical Research: Solid Earth*, *119*, 4766–4786. <https://doi.org/10.1002/2014jb011058>
- Wentzcovitch, R. M., Tsuchiya, T., & Tsuchiya, J. (2006). MgSiO₃ postperovskite at D conditions. *Proceedings of the National Academy of Sciences of the United States of America*, *103*(3), 543–546. <https://doi.org/10.1073/pnas.0506879103>
- Wookey, J., Stackhouse, S., Kendall, J.-M., Brodholt, J., & Price, G. D. (2005). Efficacy of the post-perovskite phase as an explanation for lowermost-mantle seismic properties. *Nature*, *438*(7070), 1004.
- Wu, Z., & Wentzcovitch, R. M. (2014). Spin crossover in ferropericlase and velocity heterogeneities in the lower mantle. *Proceedings of the National Academy of Sciences*, *111*(29), 10,468–10,472. <https://doi.org/10.1073/pnas.1322427111>
- Yang, J., Lin, J.-F., Jacobsen, S. D., Seymour, N. M., Tkachev, S. N., & Prakapenka, V. B. (2016). Elasticity of ferropericlase and seismic heterogeneity in the Earth's lower mantle. *Journal of Geophysical Research: Solid Earth*, *121*, 8488–8500. <https://doi.org/10.1002/2016JB013352>
- Zhan, Z., Helmberger, D. V., & Li, D. (2014). Imaging subducted slab structure beneath the Sea of Okhotsk with teleseismic waveforms. *Physics of the Earth and Planetary Interiors*, *232*, 30–35. <https://doi.org/10.1016/j.pepi.2014.03.008>
- Zhao, D., Fujisawa, M., & Toyokuni, G. (2017). Tomography of the subducting Pacific slab and the 2015 Bonin deepest earthquake (Mw 7.9). *Scientific Reports*, *7*, 44487. <https://doi.org/10.1038/srep44487>